

Playing on 3D spatial distribution of Cu-Co (oxide) nanoparticles in inorganic mesoporous sieves: impact on catalytic performance toward the cinnamaldehyde hydrogenation.

Carmen Ciotonea,^{a,b,c*} Alexandru Chiriac^b, Brandusa Dragoi,^b Jeremy Dhainaut,^a Maya Marinova,^c Stephane Pronier,^d Sandrine Ariei-Clacens,^d Jean-Philippe Dacquin,^a Emil Dumitriu,^b Adrian Ungureanu,^{b,*} and Sébastien Royer,^a

^a Univ. Lille, CNRS, Centrale Lille, Univ. Artois, UMR 8181 – UCCS – Unité de Catalyse et Chimie du Solide, F-59000 Lille, France.

^b "Gheorghe Asachi" Technical University of Iasi, Faculty of Chemical Engineering and Environmental Protection, 73, Prof. D. Mangeron Bvd., 700050 Iasi, Romania.

^c Univ. Lille, CNRS, INRA, Centrale Lille, Univ. Artois, FR 2638 – IMEC – Institut Michel-Eugène Chevreul, 59000 Lille, France..

^d Université de Poitiers, CNRS UMR 7285, IC2MP, 4 Rue Michel Brunet, 86022 Poitiers Cedex, FRANCE

Corresponding authors: Tel. +33 (0)3 20 05 87 40, email address. carmen.ciotonea@univ-lille.fr (Carmen Ciotonea); Tel. +40 (0)2 32 27 86 83; email address. aungureanu@tuiasi.ro (Adrian Ungureanu)

ABSTRACT

The preparation of supported bimetallic materials based on transition metals has attracted much interest since their use as catalysts towards hydrogenation processes for the production of fine chemicals or environmental depollution processes. The synthesis procedure proposed in this study allows to obtain bimetallic materials with high dispersion of the active sites, control of the chemical composition and localization as well as good thermal resistance against sintering. In this line, a series of materials based on Cu and Co supported on SBA-15 were prepared by the optimization of the drying step during incipient wetness impregnation, the ratio of Cu-Co was studied and the monometallic materials were used for comparison. The physico-chemical properties of freshly calcined and reduced materials were investigated by ICP-EOS, nitrogen physisorption, ex-situ and in-situ XRD, TEM-EDX, TPR and XPS. The materials showed improved dispersion at low copper ratio, due to the stabilization

of $\text{Cu}_x\text{Co}_{(1-x)}\text{Co}_2\text{O}_4$ spinel phase, promoting a high dispersion of confined NPs of 9 nm within the large pores of the SBA-15. Subsequent stabilization of the Cu and Co NPs is observed by in situ-XRD, and the collected HAADF micrographs clearly evidence a high dispersion of the copper within the bimetallic NPs. However, when copper is exceeding the CuCo ratio of 4:1, larger NPs of CuO located outside the silica mesopores are observed. Subsequent catalytic performances were investigated in the hydrogenation reaction of cinnamaldehyde (CNA), in two different pressure regimes (1 bar and 10 bars). For the reaction under pressure, CuCo1:4 showed the highest conversion with 67 mol % after 150 min of reaction, while the selectivity to the cinnamyl alcohol (CNOL) was of 47 mol %. The same catalyst showed a conversion of 99 mole % in atmospheric pressure after 24 h of reaction and the selectivity to CNOL reached 72 mole %. Such results confirm that our modified IWI protocol using mild drying step is valuable towards the preparation of confined bimetallic nanoparticles within mesoporous sieves. High stability of such confined nanoparticles allow reduction of the active elements up to the metallic state, which strongly promotes the catalytic performance towards CNA hydrogenation reaction.

Keywords: transition metal oxide, mesoporous support, supported catalyst, bimetallic catalyst, hydrogenation reaction

• INTRODUCTION

The design of supported metal nanoparticle catalysts has attracted considerable interest in various catalytic applications of heterogeneous catalysis [1] where the necessity of using more than one type of metallic active sites is often requested due to the complexity of the studied reactions [2]. Therefore, numerous research groups focused their work on the preparation methods and/or applications of (bi)metallic supported nanoparticles (NPs) as catalysts in various (de)hydrogenation processes involved in important fields such as fine chemistry, environmental pollution control, energy and so on [3]. As reported in literature, the insertion of a second active metal to the catalytic phase has the capacity to boost the properties of the first metal due to the modification of its electronic properties [1-4]. In this line, non-noble (bi)metallic supported nanoparticles (NPs) (e.g. Ni, Cu, Co...) offer a variety of technical and commercial advantages, which make them feasible substitutes to the more expensive supported noble metal NPs (e.g. Pt, Pd, Ir, Au)[4]. The particular NPs morphology (shape and size) and their chemical composition (affecting the metal-support and metal-reactant interactions) are the main variables which affect the catalytic activity of supported bimetallic NPs. Consequently, by optimizing the dispersion and accessibility of the active metal species, greatly enhanced catalytic performances of supported NPs (i.e. activity and selectivity) have been reported with respect to their bulk counterparts. Those observations can be explained

by larger surface-to-volume ratios of NPs (i.e. higher dispersion) associated with an increased number of defect sites, kinks, steps, edges and corners [5]. Therefore, considerable research efforts are focused nowadays on the development of new preparation methods which can produce such advanced catalytic nanomaterials via both physical and chemical approaches [2-5]. To reach the production of NPs with similar physico-chemical properties, it is desirable to use a support with ordered array of pores and high surface area, in order to get a better control in the NPs deposition and an easier understanding of the stabilisation processes that took place during the preparation and activation of the catalyst. Among the candidates fitting all the above conditions, the SBA-15 presents a highly ordered mesoporous siliceous skeleton with advanced characteristics comparable to other silica homologues[6], and makes it ideal to be used as host structure: (i) high specific surface areas ($600-1000 \text{ m}^2\text{g}^{-1}$); (ii) high (hydro)thermal stability with respect to its MCM-41 counterpart, well defined pore structure formed of hexagonal array of large and tunable cylindrical pores (diameter 5-10 nm) which allow the confinement of NPs and also a very good thermal stabilisation towards particle sintering [7]. Also a secondary porosity can be produced and, in this case, small particles may be immobilized onto the support porosity, resulting in a material with enhanced properties in term of stabilisation and dispersion. [8-11]

By far the most frequently used method in both academy and industry for the preparation of supported NPs is the incipient wetness impregnation technique (IWI), due to some essential sustainability-related characteristics such as versatility [12-14], convenience, low amount of required solvent, availability and low cost of metal sources, high purity of metal precursor phases and limited production of waste. Being easy to obtain, the principle of IWI method [28] is to mix an aqueous metal source with a porous support, followed by drying and thermal decomposition and/or reduction of the precursors to obtain the oxide phase [15].

Bi-metallic materials based on Cu and Co NPs are very interesting to be studied as a potential synergic catalytic system. The copper is located in periodic table, within the 11th transition metal group. The specificity of this group is that the “d band” is fully occupied. Thus, copper is expecting to manifest less affinity for accepting electrons and consequently, we should observe poor selectivity under the hydrogenation reaction. Interestingly, copper, as well as the other elements from the 11th group are showing very good selectivity toward the hydrogenation of C=O band of α,β -unsaturated aldehydes [4]. On the other side, cobalt is located in the 9th group, thus partially filled d band, and is showing excellent selectivity toward the production of unsaturated alcohol from the hydrogenation of citral, acetophenone and cinnamaldehyde [16].

Regarding the literature, Cu and Co bi-metallic materials were deposited onto various supports such: SiO₂ [17-18], Al₂O₃[19] TiO₂[20-21] porous carbon [22], etc. In an attempt to summarize the above observations, three situations can be found on solids based on Cu-Co supported on silica: formation of single monometallic oxides of *i)* large CuO NPs; *ii)* the spinel Co²⁺₁Co³⁺₂O₄ NPs or *iii)* combination of both Co and Cu within the bimetallic spinel, with general formula Cu_xCo_(3-x)O₄ [23-25]. The Co₃O₄ spinel belonging to the space group *Fd3m* has one-eighth of the tetrahedral sites occupied by Co²⁺ cations, while one half of the octahedral sites are occupied by Co³⁺ cations, consequently, the insertion of Cu²⁺ within the spinel will take place in the tetrahedral position of Co²⁺ as follow Cu_xCo_(1-x)Co₂O₄, where x can have only values inferior to 1.[23, 25-28].

Albeit IWI is often considered as a straightforward way to produce metal NPs, numerous results are showing a heterogeneous distribution of the single oxides and high amount of external large particles, thus there is space to improve the IWI procedure [29].

Accordingly, our undertaking research is motivated by the possibility to optimize the procedure of the IWI method in order to outcome a general, controlled/reproducible and facile impregnation approach to prepare transition (bi)metallic NPs supported on SBA-15. Herein, we report the synthesis of CuCo NPs stabilized within the ordered mesoporosity of SBA-15 silica through a modified incipient impregnation method including mild drying step (25°C, ±2°C). In this context, our objectives are the exploitation of factors that affect the physico-chemical properties of non-noble bimetallic nanoparticles (Cu and Co) supported on SBA-15 for enlarging the geometric and electronic features such as the particle size and morphology, the nature of the two metals and their electronic behavior influencing the metal-reactant interactions. For the latter properties, the reactivity of CuCo NPs supported onto SBA-15 has been evaluated towards the hydrogenation of cinnamaldehyde (CNA). The chemoselective hydrogenation of α,β-unsaturated aldehydes is very sensitive to the behaviour of the divided phases [4]. Within this family of reactions, the selective production of cinnamyl alcohol (CNOL) by hydrogenation of cinnamaldehyde (CNA), is highly sought for, because the unsaturated alcohol is an important additive in pharmaceuticals, agrochemicals, flavours and fragrances. For that reason, hydrogenation of CNA draws increased attention in the fine chemical sector as one of the current challenges to be tackled from both fundamental and industrial viewpoints. In industry the production of cinnamyl alcohol is realised by Meerwein-Ponndorf –Verley reduction, while the catalytic processed is realised by using OsC as catalyst [30-31]. The main difficulty arises from the hydrogenation of C=C bond that is thermodynamically and kinetically favoured [32] and thus the saturated hydrocinnamaldehyde (HCNA) is usually the major by-product. Furthermore, a competition reaction took place for the hydrogenation to the second unsaturated bond from either the unsaturated alcohol or the saturated

aldehyde already formed, subsequently the saturated hydrocinnamyl alcohol (HCNOL) is produced (Scheme 1, SI file).

Until now, Cu-Co supported on silica were previously used in the hydrogenation of α,β -unsaturated aldehydes, with good conversion up to 50 % and high selectivity. The necessity of the copper into the bimetallic system is due to the fact that the latter is favouring the hydrogen dissociation, while the adsorption of the cinnamaldehyde will take place onto the active sites of M^{2+} (with $M^{2+} = Cr, Co, etc$) via η^1 on top adsorption, thus the presence of the sites formed by Cu^0M^{2+} are preferred to be used for the CNA hydrogenation toward the enhancement of unsaturated alcohol [4,33].

In our method, the main results dealing with the chemoselectivity of the reaction will be discussed and linked with geometric and electronic features which are in close relationship with the physico-chemical properties of the porous host in which the bimetallic NPs are stabilized.

• EXPERIMENTAL

2.1. Catalyst preparation

Materials: All chemicals required for the synthesis of the mesoporous silica support and derived supported metal catalysts were used as purchased: tetraethylorthosilicate ($Si(OC_2H_5)_4$, TEOS-98 wt.%, Sigma-Aldrich), non-ionic triblock copolymer Pluronic P123 (poly(ethyleneoxide)-block-poly-(propyleneoxide)-block- poly(ethyleneoxide)-block), $EO_{20}PO_{70}EO_{20}$, molecular weight of 5800, BASF Corp.), hydrochloric acid (HCl, 37 wt.%, Sigma-Aldrich), cobalt nitrate ($Co(NO_3)_2 \cdot 6H_2O$, 98 wt.%, Sigma-Aldrich) and copper nitrate ($Cu(NO_3)_2 \cdot 3H_2O$, 98 wt.%, Sigma-Aldrich). For the catalytic runs, the chemicals were also used as received: trans-cinnamaldehyde ($C_6H_5CH=CHCHO$, 98 wt.%, Merck) as reagent, propylene carbonate ($C_4H_6O_3$, 99 wt.%, Sigma-Aldrich) and isopropanol (C_3H_8O , Merck 99 wt.%) as solvents.

Support synthesis: Ordered mesoporous SBA-15 support was prepared by using chemical acidic conditions [34] of HCl (1.6 M) by using Pluronic P123 (4 g). The resulting mixture was treated at 40 °C. After complete dissolution of the structure directing agent, the silica source, TEOS (8.5 g), was added dropwise to the solution, followed by magnetic stirring for 24 h at 40 °C. A hydrothermal treatment for 48 h at 100 °C was used for consolidation of the gel. The hybrid solid was recovered by filtration, washed, and dried under air. In order to obtain free porosity, the material was calcined at 550 °C for 6 h (in a muffle furnace, using a heating ramp of 1.5 °C min⁻¹).

IWI method: Transition metal oxide-loaded SBA-15 samples were prepared by incipient wetness impregnation under mild drying conditions [15]. The volume of TM precursor aqueous solution added for IWI-MD is equal to V_p measured by N_2 physisorption for the parent SBA-15 used. The equivalent of aqueous metal nitrate precursors solutions were mixed for achieving a constant loading of zero-valent metal components of 5 wt.% and variable Cu/M weight ratio (in the range of 0 - 5; $M = Cu + Co$). The solution containing solids was gently dried under air at 25 ± 1 °C for 48 h. As previously showed by our group, dry step performed at room temperature is improving the dispersion of the NPs compared to classical IWI (drying step at 100°C). The powders were thereafter calcined under air at 500 °C for 6 h (heating ramp of 1.5 °C. min^{-1}) to obtain the oxidic form of catalysts. To avoid the “container effect” during calcination, open crucibles and similar sample depths were used. After calcination, the solids were stored under ambient conditions in sealed containers. The monocomponent and bicomponent samples were labelled according to their chemical composition as $CuCo_{x:y}$, where x:y are namely Cu and Co in relative proportions (x:y = 5:0, 1:4, 1:1, 4:1, 0:5).

2.2 Materials characterisation: Materials were systematically characterized in their oxidized and/or reduced state using XRD at low and ex-situ and in-situ large angles, nitrogen physisorption, TEM-EDX, TPR, XPS and ICP-OES. Catalytic tests were performed after a reduction treatment at 500 °C in order to evaluate the beneficial impact of the metallic preparation on catalytic potential of the final materials.

ICP-OES analyses were performed using a sequential scanning inductively coupled plasma with an optical emission spectrometer (Perkin Elmer Optima 2000 DV) to determine the chemical composition of the samples. Before analysis, a known amount of sample was dissolved in a diluted HF-HCl solution under microwave heating. Results showed that transition metal final loading is slightly higher than the expected 5 wt.% value.

N_2 -physisorption isotherms were recorded at -196 °C on an Autosorb 1-MP automated gas sorption system (Quantachrome Instruments). Before analysis, the samples were outgassed under dynamic vacuum at 350 °C for 3h. Textural properties were determined from the adsorption/desorption isotherms by using the Autosorb 1 software. BET surface area was determined using the multipoint BET algorithm in the P/P_0 range of 0.1-0.25. The t-plot method was applied to quantitatively determine the micropores volume and surface areas (de Boer statistical thickness P/P_0 of 3.8-6.5 Å). The mesopore size distribution was determined by NLDFT equilibrium algorithm applied for cylindrical pores.

Micrographs (transmission electron microscopy, TEM) on oxidized samples were recorded on a JEOL 2100 UHR instrument (operated at 200 kV with a LaB6 source and equipped with a Gatan Ultra scan camera), with a resolution

of 0.19 nm, and equipped with an Energy Dispersive X-ray Spectroscopy (EDXS) detector. All the samples were embedded in a polymeric Epoxy resin (spurr) and cut into sections of 50 nm using an ultramicrotome equipped with a diamond knife. Cuts were deposited on gold grids in order to get proper information about the copper content from the samples when analysing. The images on samples reduced at 750 °C were collected on a TITAN Themis 300 S/TEM with a probe aberration corrector and monochromator, allowing spatial resolution of 70 pm and energy resolution of 150 meV. The microscope was equipped with a super-X windowless 4 quadrant SDD (silicon drift detector) detection system for the STEM-EDX mapping and with several annual dark field detectors. The experiment was performed with a 0.5 nm probe size, a convergence angle of 21 mrad and a probe current of approximately 100 pA. For the high angle annular dark field (HAADF), images collection angles have been between 50 and 200 mrad.

X-ray diffraction was performed using PANalytical Empyrean X-ray diffractometer, in Bragg Bentano configuration, with Cu K radiation ($\lambda = 1.54184 \text{ \AA}$). For small-angle analysis, diffractograms recorded for the data were collected in the 2θ ranging from 0.5° to 5° , with a step size of 0.01° . Wide-angle analyses were performed for a 2θ range, laying between 10° and 80° with a step size of 0.05° . Mean crystal size was calculated using the Scherrer equation: $D_{hkl} = K \cdot \lambda / b \cdot \cos\theta$, where K is a structure constant (0.9, for spherical crystals); λ is the incident ray wavelength; b is the peak width at half height after correction for instrumental broadening; and θ is the Bragg angle. Powder XRD: patterns were recorded on a Bruker D8 ADVANCE X-ray diffractometer equipped with a VANTEC-1 detector, using a Cu K α radiation ($\lambda = 1.54184 \text{ \AA}$) as X-ray source. The calcined samples were placed on a kanthal filament(FeCrAl) cavity, and were subjected to thermo-programmed reduction under a flow of 3.0 vol.% H₂ in He (30 mL min⁻¹) from 30 °C to 500 °C (heating ramp of 5 °C min⁻¹). The in situ diffractograms were recorded at definite temperatures in the 2θ range from 15 to 70° with a step of 0.05°. Crystal phase identification was made by comparison with ICDD database.

Temperature-programmed reduction under H₂ (H₂-TPR) was conducted on an Autochem chemisorption analyser (Micromeritics), equipped with a TCD. The consumption of H₂ was driven from the TCD signal after calibration. Prior to the H₂-TPR run, the solid was activated up to its calcination temperature (from room temperature to 500 °C, heating ramp of 5 °C min⁻¹, and isothermal time of 1 h) under simulated air at a total flow rate of 30 mL min⁻¹. After cooling down to 50 °C, the H₂ containing flow was stabilized (30 mL min⁻¹, 3.0 vol.% H₂ in Ar) and the temperature-programmed reduction was performed (from 50 °C to 900 °C, with a temperature ramp of 5°C min⁻¹).

X-ray photoelectron spectroscopy (XPS) analyses were performed with a Kratos Axis Ultra, equipped with a dual Mg/Al anode and a monochromatized Al K α source (1486.6 eV). The samples were analyzed as pellets, mounted on a double-sided adhesive tape. The pressure in the analysis chamber was in the range of 10⁻⁹ mbar during data registration. The binding energies were referred to the C1s component positioned at 284.8 eV. Atomic concentrations were calculated from peak intensity using the sensitivity factors provided with the Casa XPS software (version 2.3.16 PR 1.6). The binding energy values are quoted with a precision of ± 0.15 eV and the atomic percentage with a precision of $\pm 10\%$.

2.3. Hydrogenation reaction of cinnamaldehyde

Performance in catalysis - **at atmospheric pressure**: liquid phase hydrogenation of cinnamaldehyde was performed in a three phase system, in a thermostatic three-neck glass reactor equipped with reflux condenser, hydrogen bubbler and magnetic stirrer. The following reaction conditions were applied: temperature of 150 °C, 1.05 g of trans-cinnamaldehyde, 25 mL of propylene carbonate, 0.265 g of activate catalyst, hydrogen flow of 1 L h⁻¹, and stirring rate of 900 rpm.

-at high-pressure: liquid phase hydrogenation of cinnamaldehyde reaction was performed by using a Parr reactor under the following typical conditions: 1 mL cinnamaldehyde, 40 mL isopropanol as a solvent, 0.133 g catalyst, 10 bar H₂ and reaction temperature of 130 °C.

Prior to the catalytic runs, the calcined samples were gently crushed and sieved to obtain a granulometric fraction lower than 0.126 mm. Transition metal oxide phases, obtained after calcination of the materials, were then reduced to the metallic form at 350 °C and 500 °C for 10 h (heating ramp of 6 °C min⁻¹) under H₂ flow (1 L. h⁻¹). Preliminary tests made with different granulometric fractions and loadings of catalyst, and different stirring rates, disclosed no diffusional limitations under the selected reaction conditions. Aliquots of reaction mixture were withdrawn periodically and analysed by gas chromatography (HP 5890 instrument, equipped with a DB-5 capillary column and a FID detector). The identification of the reaction products was achieved from the known retention times of pure compounds and occasionally by GC-MS (Agilent 6890N system equipped with an Agilent 5973 MSD detector and a DB-5-ms column). The conversion of cinnamaldehyde and selectivities in the different hydrogenation products were calculated by taking into account the FID response factors for each compound.

3. RESULTS AND DISCUSSION

3.1 Surface area and porosity

The adsorption/desorption isotherms and related pore size diameter distributions of supported CuCo NPs on SBA-15 were registered by N₂ physisorption at -196 °C and are presented in Figure 1. Corresponding textural properties are summarized in Table S1. For all freshly calcined materials, isotherms of type IV with H1-type hysteresis loops are easily observed, which evidence the presence of highly ordered mesoporous silica type SBA-15 with cylindrical channels. Parallel branches of the hysteresis loop are indicating a uniform periodic arrangement of the mesopores, as it can be also noticed by the derived pore size distribution (figure 1). A latency can be observed in closing of the hysteresis which arises from the presence of NPs inside the channels. Such pore blockages induce the formation of ink-bottle shape pores, visible onto the hysteresis (i.e. on the desorption branch side) at pressures ranging from 0.58 to 0.78 [35]. The pore size distribution, from NL-DFT model, is showing an uniform pore size distribution of 8.4 nm and are in close agreement with the low angle XRD patterns (Figure S1). The presence of NPs inside the mesoporosity can be first indicated by the formation of smaller mesopores of 7.3 nm. Further evidence of the NPs confinement is highlighted by the decrease of the specific surface area of the CuCo materials (from 760 m².g⁻¹ to 575 m².g⁻¹) with respect to the parent SBA-15 (880 m².g⁻¹).

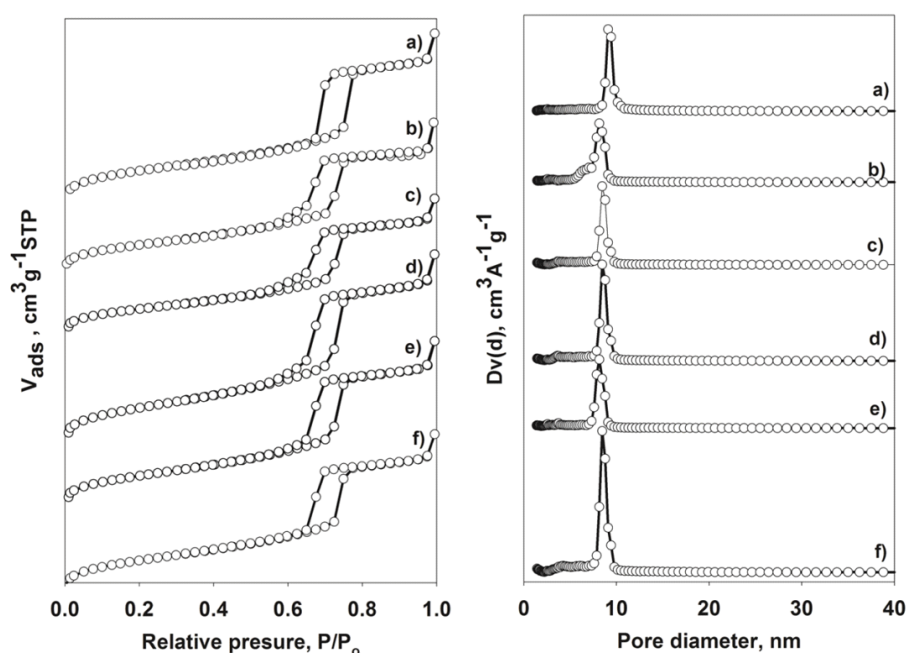


Figure 1. a) Adsorption/Desorption isotherms; b) Pore size diameter corresponding to support and Cu/Co containing materials: a) SBA-15; b) CuCo0:5, c) CuCo1:4; d) CuCo1:1; e) CuCo4:1, f) CuCo5:0.

3.2 Structure and Morphology

For all samples, low angle XRD analysis is revealing typical peaks corresponding to the planes of 100 , 110 and 220 (Figure S1). All planes are representative of a high periodic arrangement of the channels of the silica type SBA-15 and is associated to $p6mm$ symmetry. The presence of the NPs inside the mesoporosity is as well confirmed by the shift at higher 2θ for $d100$ peak which appears also less intense than the parent support, accordingly the a_0 is of 9.3 ± 0.1 nm for all the bi-metallic materials (Table S1) [15]. Wide angle XRD registered for calcined samples are presented in Figure 2. Reflections corresponding to CuCo5:0 material (figure 2-e) point out the presence of large copper oxide NPs (ICDD 48-1548), with a mean crystallite size around 32 nm evidencing a strong NPs enrichment on the external surface of SBA-15 granules. When switching from CuCo 5:0 to CuCo 0:5 solid, a significant mitigation of the reflexion lines occurs, suggesting a better distribution of cobalt oxide NPs within the mesoporosity of the silica. Co_3O_4 phase was further identified by comparison with the reference (ICDD 42-1467) and NPs size was estimated around 9 nm. For mixed CuCo ratios, the observed diffraction patterns did not allow us to discriminate Co_3O_4 phase from $\text{Cu}_x\text{Co}_{(1-x)}\text{Co}_2\text{O}_3$ phase, [36] which are both exhibiting very close 2θ values. Besides, the CuCo bimetallic solids present diffraction patterns which can be assigned to CuO and spinel phases, all displaying different relative intensities in agreement with the ratio of Cu and Co requested for the preparation (figure 2).

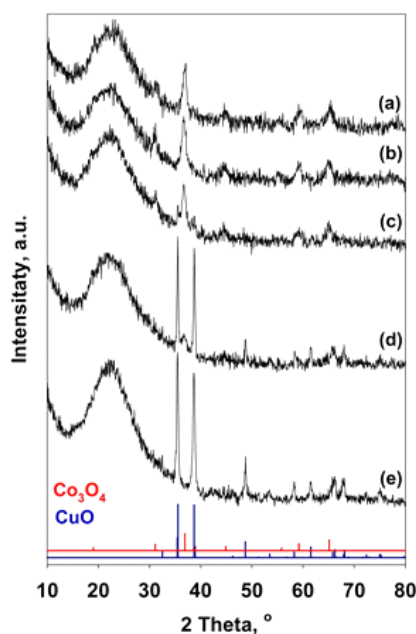


Figure 2. Wide angle XRD patterns for: (a) CuCo0:5; (b) CuCo1:4; (c) CuCo1:1; (d) CuCo4:1; (e) CuCo5:0; bottom: in blue CuO (pdf No: 48-1548) and in red Co_3O_4 (pdf No: 42-1467).

It is interesting to note that a slight decrease in crystallite size of the spinel phase is observed when decreasing the amount of copper (from 9.0 nm (CuCo4:1) to 8.1 nm (CuCo1:1)). For CuCo4:1 small crystallites of 7 nm for

Co_3O_4 are obtained but very large CuO particles are formed with a size of 29 nm, as evidenced by the presence of very sharp reflection lines. Such results confirm that CuO particles are located outside of the SBA-15 mesoporosity. Representative TEM and HAADF analyses together with the EDX analysis were performed to provide deeper insight about the morphology, the dispersion and the chemical composition of the Cu and Co elements for freshly calcined materials (Figure 3, 4, S2, S3 and S4). First, monometallic supported oxides ($\text{CuCo}_{5:0}$ and $\text{CuCo}_{0:5}$) exhibit different features with respect to their mixed oxide counterparts. As seen in figure S2, a distribution of polycrystalline cobalt oxide particles is clearly noticed as nanorods inside the SBA-15 mesoporosity for the $\text{CuCo}_{0:5}$ sample, while the single copper sample is showing a majority of large aggregates located outside the support porosity. Local EDX analyses were realized on selected regions from TEM images and are illustrated in Figure S3. The large particles found outside the SBA-15 are assigned to copper oxide particles (S3 1,3). Now, when analysing the distribution of copper oxide nanoparticles for $\text{CuCo}_{4:1}$, $\text{CuCo}_{1:1}$ and $\text{CuCo}_{1:4}$ samples, we noticed that higher the amount of copper is, the larger particles are found (> 50 nm) outside the support porosity of silica (Figure 3). The main reason of such observations can be assigned to the high mobility of copper particles rendering its stabilization difficult on a silica type support because of the weak metal-support interactions [16].

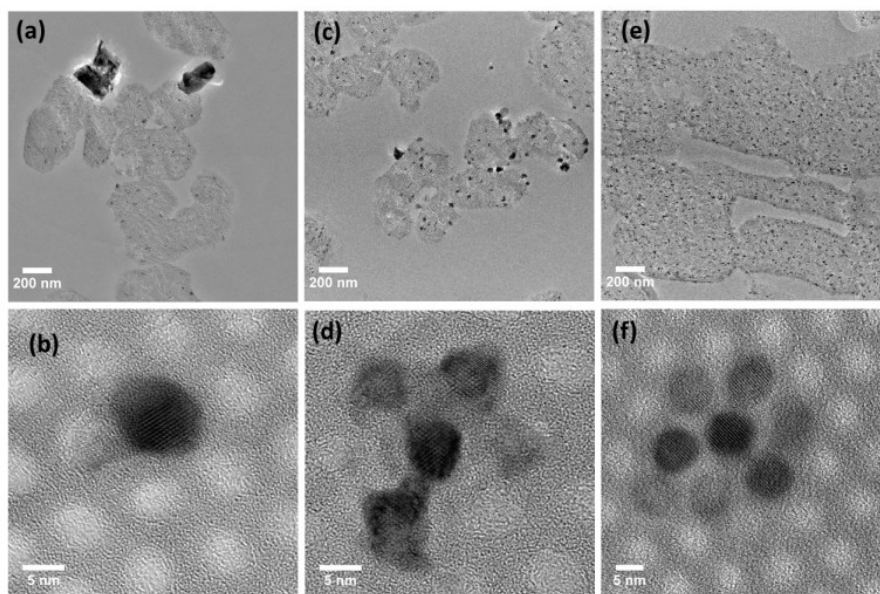


Figure 3. TEM images corresponding to: (a,b) $\text{CuCo}_{4:1}$; (c,d) $\text{CuCo}_{1:1}$; (e,f) $\text{CuCo}_{1:4}$.

On the contrary, $\text{CuCo}_{1:4}$ exhibits no visible CuO NPs outside the mesoporosity (see figure 3-e), suggesting the successful insertion of copper species within the spinel structure. It is possible to find cobalt either in pure Co_3O_4 or in partially substituted $\text{Cu}_x\text{Co}_{(1-x)}\text{Co}_2\text{O}_3$ spinel phase (see figure S3 and S4). Local analysis by EDX is

confirming XRD patterns with the presence of the spinel oxides containing copper which are visible as confined NPs within the mesoporosity of the silica (figure 3e,f and S4).

Hence, it is interesting to note that the presence of cobalt is improving the insertion of copper within the spinel phase. On the other side, the dispersion of cobalt oxide NPs throughout the porous matrix is visibly improved by decreasing progressively the copper ratio. (Fig. 3 (e,f)). As observed, the NPs size is slightly decreased from 10 nm for pure Co_3O_4 to 6.8 nm for $\text{CuCo}1:4$ (Table S1). Complementary results were collected on three unique particles with different Cu-Co ratios (figure S4) from (HR)TEM, Fast Fourier transformation (FFT), EDX analysis and ICP-EOS. As observed by FFT/EDX, the plans associated to the spinel oxide are visible for $\text{CuCo} 4:1$, $\text{CuCo} 1:1$ and $\text{CuCo} 1:4$. Such plans allowed us to depict the 3D illustration of the planar disposition of the atoms (figure S4, FFT). Hence, the FFT data is associated to the typical cubic geometry of the $Fd3m$ space group for all the three particles. However, the planar distances corresponding to the CuCo or Co_3O_4 spinel give similar values which avoid us to clearly identify the localisation or the distortions eventually generated by the enclosure of copper species in the tetrahedral sites of Co^{2+} . Finally, ICP analysis of the materials (presented in the Table S1 and figure S4) is showing a good match between experimental values and the theoretical ones corresponding to the quantity of transition metal used during the preparation. Nevertheless, the EDX analysis on the single particles (figure S4) is indicating atomic percentages of cobalt from 57 at.% to 88 at.% and for copper from 43 at.% to 12 at.%. Knowing that the percentage of copper for the full substitution within $\text{Cu}_x\text{Co}_{(1-x)}\text{Co}_2\text{O}_3$ is of 12.5 atoms, we can presume that all Co^{2+} sites are substituted by the copper species in $\text{CuCo}1:4$ sample (figure S4) [25-28]. In the case of $\text{CuCo}1:1$ and $\text{CuCo}4:1$, knowing that Cu^{2+} species are exceeding 12 at.%, the copper is favoured to be found as copper oxide decorating the surface of the spinel.

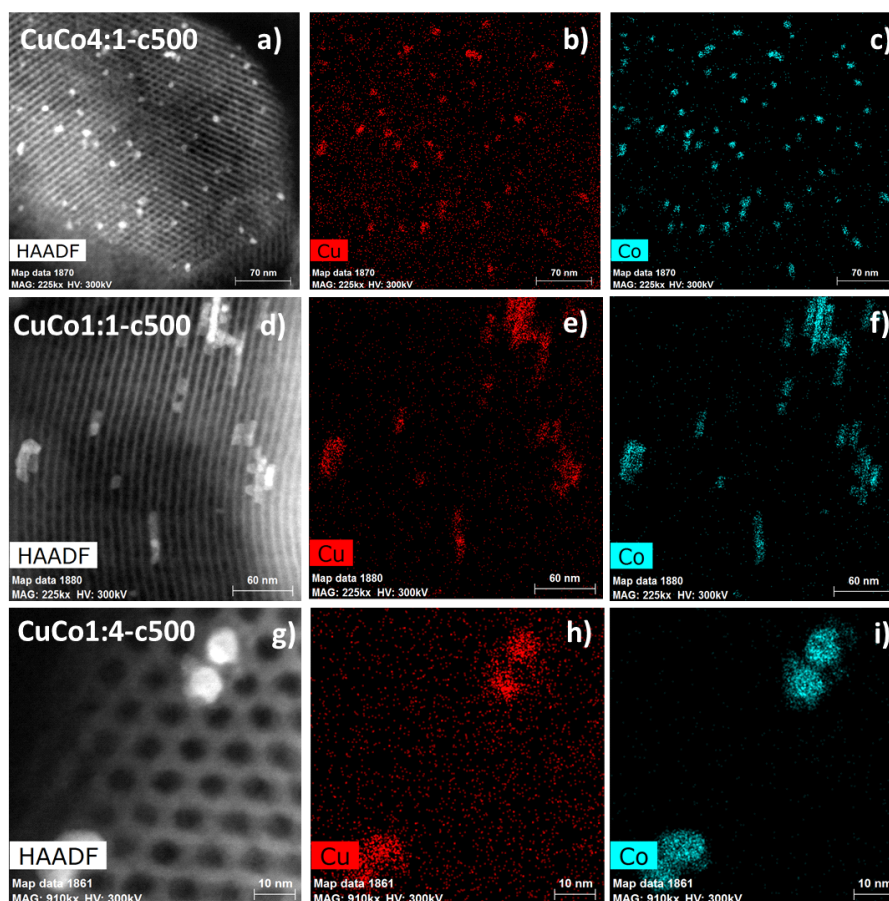


Figure 4. (a,d,g) Representative HAADF images obtained for calcined CuCo based materials; (b,e,h) copper localization as determined by STEM-EDX mapping analysis; (c,f,i) cobalt localization as determined by STEM-EDX mapping analysis.

To have more precise and local information about the copper and cobalt dispersion within the spinel and over the SBA-15 support, elemental mapping- EDX was realized on the calcined solids and the results are showed in figure 4. For all ratios, the confined NPs are composed of both Cu and Co, confirming again the formation of the $\text{Cu}_x\text{Co}_{(1-x)}\text{Co}_2\text{O}_3$ spinel phase. Besides, it is interesting to observe for all samples a population of small copper NPs (figure 4b,e,h) well distributed throughout the surface of the silica.

3.3. Reducibility properties

H_2 -TPR profiles were monitored in order to probe the temperature reduction domains of the different supported mono- and bi- metallic materials (figure 5). For the Co_3O_4 sample (CuCo 0:5), a classical two-step reduction process takes place with the occurrence of two distinct consumption ranges between 200 and 350 °C (Co(III) to Co(II) reduction) and between 350°C and 650°C (Co(II) to Co(0) reduction). The second reduction domain can be assigned to large particles situated at the external surface of the SBA-15 support, poorly dispersed, with a

maximum reduction peak at 540 °C attributed to the presence of confined Co_3O_4 NPs [24, 37]. On the other side, the profile reduction of monometallic copper oxide presents two peaks at 284 °C and 380 °C respectively, both confirming the presence of large aggregates of CuO clusters. [15]

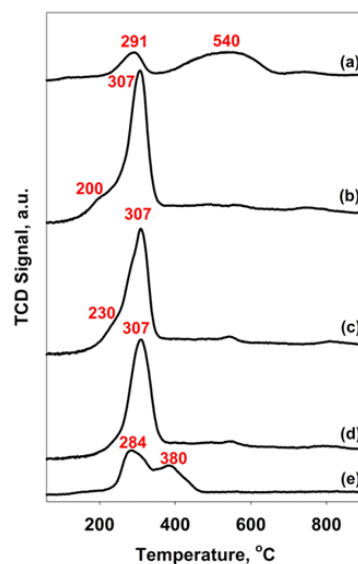


Figure 5. TPR profiles for: (a) CuCo0:5; (b) CuCo1:4; (c) CuCo1:1; (d) CuCo4:1; (e) CuCo5:0.

As observed in the case of our previous study based on CuNi systems [15], an intermediate situation is found for the bimetallic CuCo materials. Albeit a main reduction peak, located at ~ 307 °C, can be attributed to the simultaneous reduction of cobalt cations from $(\text{Cu}_x\text{Co}_{(1-x)}\text{Co}_2\text{O}_4)$ spinel phase, a clear shoulder is visible at lower temperature domains between 200 °C and 230 °C and is related to the reduction of well dispersed copper inserted into the spinel phases as previously observed by XRD and TEM (Figures 2 and 4). We can also observe a small reduction domain at higher temperature (between 500°C and 600°C), suggesting the final decomposition step of spinel phases via the reduction of Co(II) in Co(0) species.

The evolution of crystalline phases and their thermal stability during the temperature reduction was monitored by in-situ DRX (figure 6 and S5). It can be seen that, in agreement with the chemical composition of the samples, the X-Ray diagrams display the peaks assigned to various crystalline phases of Cu-Co solids. For example, for the mono-metallic cobalt (figure S5), the diffraction pattern is showing the presence of Co_3O_4 exposed up to 350 °C, then the formation of CoO phase could be observed even after reduction at 600 °C. Small diffraction peaks associated to the metallic phase of Co, located at 51.5° and 75° , can be observed upon reduction above 550°C (figure S5). Its intensity increases slightly accordingly to the increase of the reduction temperature, however the intensity signal is too weak to apply the Scherrer equation, suggesting the formation of small NPs.

For CuCo1:4 and CuCo1:1 samples, it can be seen that the peak corresponding to the Cu⁰ phase ($2\theta \sim 50.2^\circ$) is already identified at 350 °C and is relatively well-defined. However, its intensity is rather constant throughout the temperature reduction range from 350 °C up to 750 °C, indicating the successful stabilization of copper onto the SBA-15 support when cobalt is added. It is interesting to note that the XRD patterns of CuCo1:4 recorded with a reduction temperature of 350 °C show weak diffraction peaks corresponding to Cu⁰ and Co⁰[24]. Taking into account the TPR profile for this sample, a significant shoulder is observed at $\sim 200^\circ\text{C}$ and is likely due to the reduction of smaller copper species from nanoparticles of $(\text{Cu}_x\text{Co}_{(1-x)}\text{Co}_2\text{O}_4)$ spinel, which are not detected by in-situ XRD at 250°C.

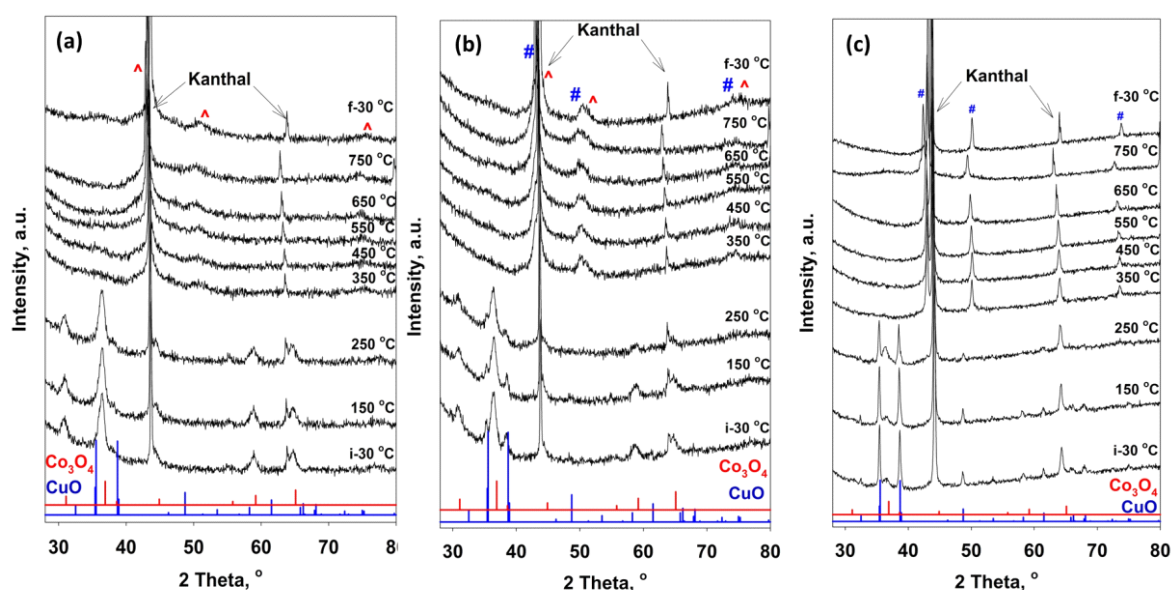


Figure 6. In-situ XRD patterns for: (a) CuCo1:4; (b) CuCo1:1; (c) CuCo4:1; bottom ICDD reference for CuO (pdf No: 48-1548) and Co₃O₄ (pdf No: 42-1467); (#-Cu⁰ and ^- Co⁰).

For CuCo4:1, the diffraction pattern is indicating very intense peaks for CuO crystalline phases, in well agreement with the TEM images. The cobalt oxide peaks are having very low intensity, being visible only for temperatures lower than 250 °C. The presence of H₂ is revealing the metallic copper at temperatures higher than 350 °C by the appearance of characteristic peaks. Moreover, any peaks corresponding to metallic cobalt cannot be identified in XRD patterns, indicating their high dispersion. A ratio of 1:1 between the two elements (CuCo1:1) leads to a slight increase in the amount of copper that is not involved in spinel phase. For the pure cobalt-based sample, similar diffraction peaks were found with respect to CuCo1:4.

Effective localization and elemental composition of the NPs, after their progressive reduction in H₂ up to 750 °C, were registered by TEM and HAADF analyses for all bimetallic materials. A complementary EDX analysis was used in order to have local information about the analytical composition. Selected images corresponding to the

Cu-Co materials are illustrated in Figure 7 and 8 and the corresponding EDX analysis are found in Figure S6. For all bimetallic materials, the presence of confined NPs can be observed after reduction under hydrogen (Figure 7). The size of the metallic NPs is close to its oxidic counterparts, indicating a high thermal stabilisation even after reduction at 750°C.

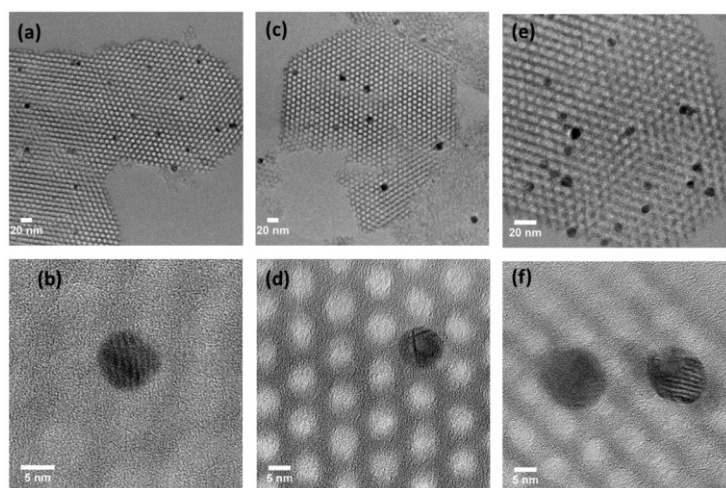


Figure 7. TEM Images collected after reduction at 750 °C for: (a) CuCo4:1; (b) CuCo1:1; (c) CuCo1:1

On the rich cobalt sample (CuCo 1:4), EDX analysis indicate the presence of the two metals in the same nanoparticle, with a mass ratio close to the theoretical one (figure S6, EDX 3). This result supports the hypothesis of heterostructures formation for CuCo 1:4 ratio. Albeit NPs contain as well both metals, different features were found in CuCo1:1 sample since different mass ratios were obtained, with experimental values being close to the theoretical one or close to copper-rich compositions, in particular in the case of nanoparticles located on the external surface. However, cumulating the TPR and TEM results, these extra-porous nanoparticles constitute a minor population. In Figure 8 are presented HAADF images as well as STEM-EDX mapping on the selected images. The results are showing that the confined NPs are maintaining a similar ratio with respect to the calcined materials. It is interesting to note that a high dispersion of copper species is present onto the silica, especially for the ratio of CuCo1:1 where the appearance of small copper NPs is revealed after the reduction. In the case of CuCo1:4, small copper based NPs are homogeneously distributed throughout the support porosity, suggesting a high dispersion which arises from a high thermal stability even after treatment in H₂ up to 750 °C. Such results confirm that the presence of cobalt is critical toward the stability of finely dispersed Cu species initially located inside the spinel structure. Moreover, the presence of cobalt is suggested to favour the formation of highly dispersed CuO NPs.

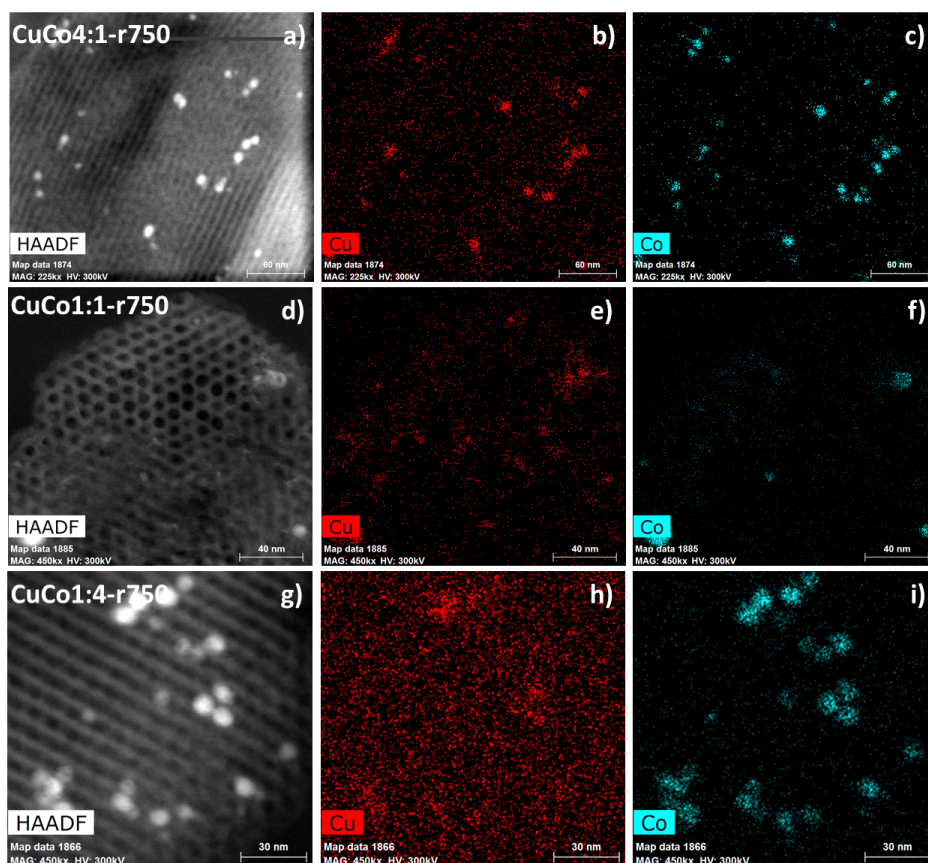


Figure 8. (a,d,g) Representative HAADF images obtained for calcined CuCo based materials; (b,e,h) copper localization as determined by STEM-EDX mapping analysis; (c,f,i) cobalt localization as determined by STEM-EDX mapping analysis.

Complementary surface information is given in Figure 9 and 10 and the spectral information from XPS are listed in Table S2 for CuCo1:4 and CuCo1:1. The materials were pre-treated under air at 500 °C prior to the temperature programmed reduction under hydrogen. The XPS spectra for Cu 2p (figure 9 and 10) registered before the reduction treatment shows the typical shake-up satellite corresponding to CuO species for the pre-treated solid, consequently the presence of the Cu²⁺ state in octahedral position is confirmed by the peak at 934.7 eV and 933.2 eV for both CuCo1:4 and CuCo 1:1. While reducing the samples at 200°C, the shake up satellite is disappearing and the main peak is becoming sharper. Hence, Cu 2p photopic is progressively shifted to 931.9 eV, which is typically associated with the presence of metallic copper species [38].

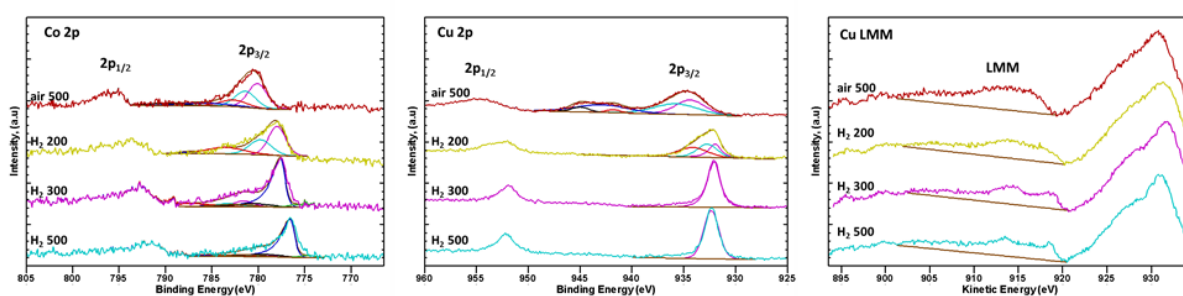


Figure 9. Core level spectra of: Co 2p (a), Cu 2p (b) Cu LMM (c) obtained for CuCo1:1 (in situ treatment under air/500°C, H₂/200 °C, H₂/300 °C, H₂/500 °C

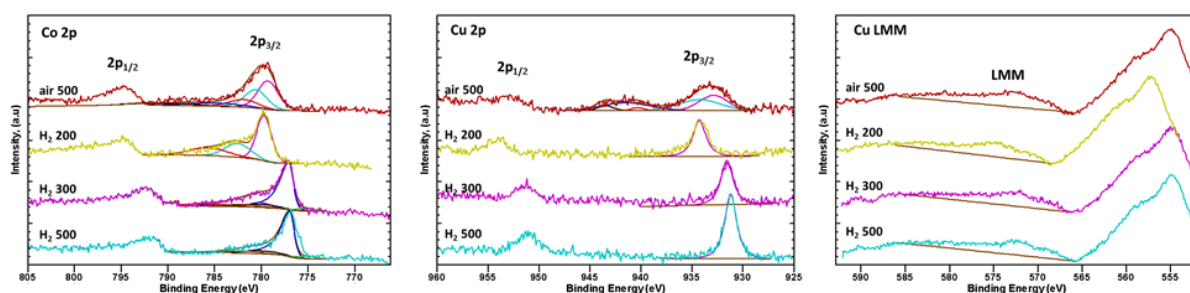


Figure 10. Core level spectra of: Co 2p (a), Cu 2p (b) Cu LMM (c) obtained for CuCo1:4 (in situ treatment under air/500°C, H₂/200 °C, H₂/300 °C, H₂/500 °C

The spectral information collected for Co 2p is showing a binding energy of 779.0 eV for Co 2p^{3/2} and 793.5 eV for Co 2p^{1/2} on the pre-treated samples. The presence of two broad shake-up satellites is also evidenced and confirms the signature of Co²⁺/Co³⁺ species from spinel Co₃O₄ phase. Upon reduction from 200 °C to 500 °C, the main photopeaks are shifted to 776.6 eV and 777.0 eV respectively, for both bimetallic samples, suggesting that the reduction is inducing the formation of the metallic cobalt species [39]. After reduction, the spectral information corresponding to Si 2p is showing the binding energy of 102.3 eV to 103.0 eV, corresponding to the presence of SiO₂, notably from SBA-15 materials, consequently the binding energies of O 1s (532.05 eV and 533.4 eV) is associated to SiO₂ support [40].

3.4 Catalytic reactivity toward cinnamaldehyde hydrogenation reaction.

The catalytic materials, obtained after appropriate reduction under hydrogen, have been tested in the liquid phase hydrogenation reaction of cinnamaldehyde using two sets of reaction conditions: (i) atmospheric pressure with a temperature of 150 °C and (ii) 10 bars with a temperature of 130 °C. Thus, the results illustrate the influence of reaction conditions and the influence of the mass ratio between the two metals on the catalytic performances.

- Results obtained for catalytic runs performed at atmospheric pressure and with a temperature of 150 °C

Conversion and selectivities obtained for all catalysts are given in figure 11-A and table 1. It can be seen that the catalytic activity of mono-metallic copper-based materials is close to zero, which is in agreement with the different structure and morphology observed for CuO NPs in CuCo 5:0 sample with respect to the bi-metallic materials.

[37] For this reason, the results about selectivity obtained on this catalyst are not relevant and are not presented herein.

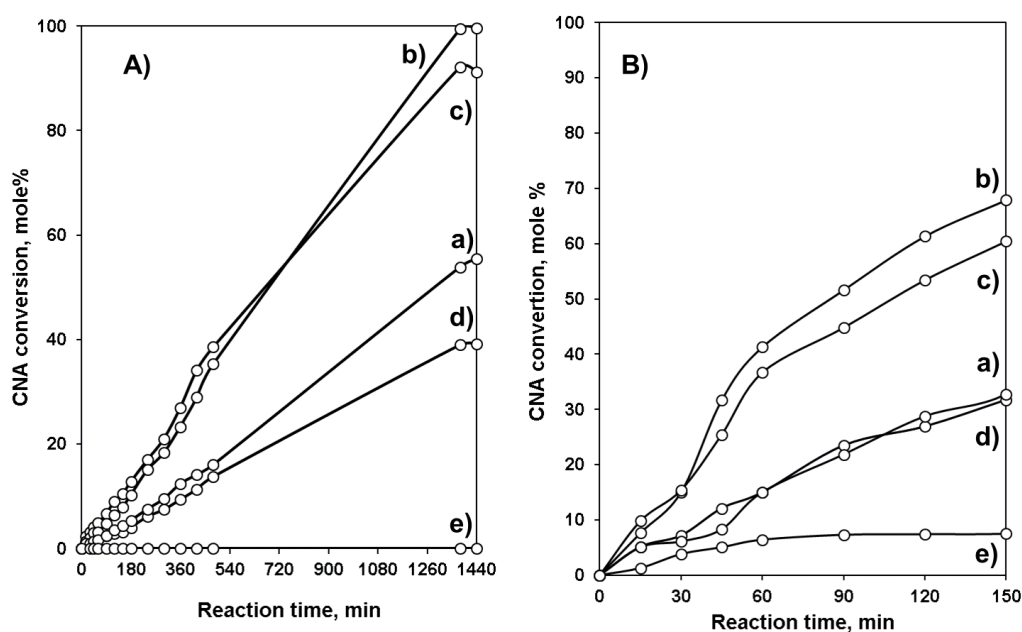


Figure 11. Catalytic activity for: (a) CuCo0:5, b) CuCo 1: 4; (c) CuCo 1:1; (d) CuCo4:1, e) CuCo5:0 ;performed at: A) Reaction conditions: $T_{red} = 500\text{ }^{\circ}\text{C}$ for sample CuCo0:5 and $350\text{ }^{\circ}\text{C}$ for the others; $T_{reaction} = 150\text{ }^{\circ}\text{C}$, 0.265 g catalyst; 1 mL CNA, 25 mL propylene carbonate as solvent, flow rate of $\text{H}_2 = 1\text{ L h}^{-1}$, speed of agitation = 900 rpm). B): $T_{red} = 500\text{ }^{\circ}\text{C}$ for sample CuCo0:5 and $350\text{ }^{\circ}\text{C}$ for other samples; $T_{reaction} = 130\text{ }^{\circ}\text{C}$, 0.133 g catalyst; 1 mL CNA, 40 mL isopropanol as solvent, agitation rate = 750 rpm.

The introduction of copper within the spinel phase clearly led to a dramatic improvement of the CNA conversion, with almost 100 mol % CNA conversion and a high selectivity toward CNOL (72 mol%) obtained for the catalyst Cu:Co1:4. These results are in accordance with the data collected from TPR, in-situ XRD and TEM on the reduced bimetallic materials, as it is considered that the decrease in catalytic activity is caused by the increase of copper particle size, especially for sample CuCo4:1. [37] In addition, since the activity of this catalyst is similar to that of mono-metallic cobalt catalyst, it is likely that the catalytic activity is mainly attributed to cobalt. Regarding now the selectivity, the hydrogenation of the C=O double bond of cinnamaldehyde seem to be favoured albeit there are no major influences of the composition and particle size on the catalytic selectivity. Thus, for sample CuCo0:5, the selectivity to CNOL at small conversions is around 80 % and it decreases gradually up to ~ 50 % with increase in conversion. Instead, for bimetallic catalysts CuCo1:4 and CuCo1:1, it can be observed a selectivity stabilized around 70 %, up to a conversion of ~ 40 %, after that it suddenly decreases. This behaviour can be explained by

the synergistic action of copper and cobalt, the latter being responsible for the increased selectivity to CNOL.[4] As reported in literature [3,4], cobalt is known to be selective for CNOL due to the width of the band d , while it is maintained to a constant value for copper. Indeed, the increasing of copper amount in the sample (CuCo4:1) decreases the selectivity towards 60 %, but its evolution with conversion follows the trend observed for the two bimetallic samples.

Table 1. Results of catalytic activities as well as the selectivities measured for the materials presented in this work.

Sample	X_{CNA}^a (mole%)	Selectivity		
		S_{CNOL}^b (mole %)	S_{HCNA}^b (mole %)	S_{HCNO}^b (mole %)
atmospheric pressure				
CuCo 0:5	55.41	69.3	19.3	12.3
CuCo 1:4	99.57	72.2	16.5	11.3
CuCo 1:1	91.2	70.6	20	9.4
CuCo 4:1	39.02	63	28.7	8.3
CuCo 5:0	0	0	0	0
10 bars pressure				
CuCo 0:5	12	72	-	-
CuCo 1:4	67	47	43	10
CuCo 1:1	60	52.6	41.2	6.2
CuCo 4:1	31	40	50	10
CuCo 5:0	0	0	0	0

a, X_{CNA} conversion measured after 24h of reaction; b, Selectivity to CNOL, HCNA and HCNO at isoconversion of CNA ($X_{CNA} \sim 12$ mol. %);

Interestingly, similar catalytic performances were obtained for the same ratio in the case of catalysts based on CuNi/SBA-15 as reported in a previous work [15]. These results suggest that (i) a ratio $M_1: M_2 = 1:4$, where $M_1 = Cu$ and $M_2 = Ni(Co)$ represents the optimum ratio at which the synergistic interactions between the two metals have positive effects on the physico-chemical and catalytic properties of materials and (ii) as also shown for the CuNi system, the bimetallic particles obtained by our approach are not classical alloys, but rather hetero-structures which share a mixed interface, with no segregation of copper on the surface of cobalt or nickel. For CuCo system, the results indicate similar catalytic behaviours as CuNi system. Additional increase of the copper amount (CuCo1:1 and CuCo4:1 samples) led to the gradual decrease in the catalytic activity.

ii) Results obtained for catalytic runs at 10 bars, 130 °C

Conversion and selectivities obtained for catalytic tests carried out at a pressure of 10 bars are shown in figure 11-B and table 1. These results can outline three conclusions: (i) in general, as compared to the results obtained at atmospheric pressure, the catalytic activity is improved for most of the samples, excepting the samples containing mono-metallic copper, (ii) the selectivity to CNOL is diminished by about 20 mole% while the selectivity to HCNA is increased by the same percentage, and (iii) the trends for decreased activity with the chemical composition and for selectivity to CNOL are maintained, irrespective of the pressure and temperature applied. By increasing the pressure from 1 to 10 bar, the conversion level of cinnamaldehyde observed at 150 min reached 67 mole% with respect to 8 mole % obtained with the 1 bar hydrogenation reaction. The conversions in both reaction conditions are following the trend: CuCo1:4 > CuCo1:1 > CuCo0:5 > CuCo4:1 > CuCo5:0. Such trend indicates the promoting effect of smaller Cu NPs confirmed by the XRD, TPR, etc.,. Besides, CuCo0:5 catalyst is showing less conversion than the bimetallic sample rich in cobalt, respectively CuCo1:4 and CuCo1:1, suggesting the beneficial effect of the small copper NPs dispersed within the $\text{Cu}_x\text{Co}_{(1-x)}\text{Co}_2\text{O}_4$ spinel. It is interesting to note that Co mean nanoparticle size remains similar for CuCo0:5 and CuCo1:4 after reduction, indicating that Cu NPs did not inhibit the catalytic performance of the bimetallic catalyst when using an optimal ratio (Cu:Co 1:4). Hence, in this case, we presume that a partial coverage of the active particles with inactive Cu species is not likely occurring as observed from STEM-EDX mapping on the observed bimetallic materials. Similar trend of Cu-Co synergy was previously attained, in the work of Reddy et al., different bi-metallic catalysts were compared (i.e. Cu-Co, Co-Ni and Ni-Cu) toward the hydrogenation of CNA. As claimed by the authors, the combination between Copper and Cobalt supported on silica led to the highest catalytic efficiency with respect to Co-Ni and Ni-Cu counterparts. The conversion level obtained by Reddy et al. reached 40 % mole albeit vapour phase hydrogenation of CNA instead of liquid phase in our work. Besides, in the work of Marchi et al [41], selective hydrogenation of CNA was investigated on copper and cobalt inserted in hydrotalcite phase containing as well Zn and Al, using the reaction conditions: 120°C, liquid phase, isopropanol. Same behavior of Cu-Co synergy was attained. As observed in our work, increase of the Cu dispersion is correlated to a higher conversion rate in the presence of cobalt without significantly modifying the selectivity of the reaction. Taking into account the above considerations, it can be shown that a catalytic synergic effect between Co and Cu is occurring when dealing with CNA hydrogenation toward CNOL production.

CONCLUSION

In this study, the preparation of Cu-Co bimetallic supported on SBA-15 materials are reported following an optimized IWI technique involving drying in mild condition. A series of 3 Cu-Co ratios were prepared, while the

monometallic materials were used for comparison. The physico-chemical properties of calcined and reduced materials were investigated by ICP-EOS, nitrogen physisorption, XRD and in-situ XRD, TEM-EDX, TPR and XPS. The insertion of Cu in small quantities has beneficial effect for gaining a high stability because copper can be inserted into $\text{Cu}_x\text{Co}_{(1-x)}\text{Co}_2\text{O}_4$ spinel phase. Thus, improved dispersion of the NPs is observed onto the mesopores of the SBA-15. When large amount of copper is used, the materials are showing large aggregates composed of CuO NPs with a size around 30 nm, while Co_3O_4 particles are showing a poor distribution throughout the porous matrix. For bimetallic materials, the reduction domains of the NPs are shifted toward low temperatures with maximum at 200°C and 307°C with respect to those observed for monometallic CuCo 0:5. Further XRD study of the bimetallic materials under reductive conditions showed that a high dispersion of Cu and Co is possible up to 750 °C, such results are confirmed by TEM and HAADF images collected after reduction at 750 °C. The impact of NPs physico-chemical properties was studied in the selective hydrogenation of cinnamaldehyde (CNA) with the objective to get high selectivity to cinnamyl alcohol. Very high conversions were obtained for CuCo1:4 and CuCo1:1, which showed a conversion of 67 mole % and 60 mole % respectively after 150 min of reaction, while the selectivity to the CNOL was of 47 mole % and 52 mole %. Under atmospheric pressure, the same catalyst showed a conversion of 99 mole % and 91 mole % after 24 h of reaction and the values obtained for selectivity to CNOL reached 72 mole % and 70 mole% respectively. This study provides new insights into the high stabilisation of copper-cobalt NPs onto SBA-15 support via a versatile preparation method. The Cu-Co based materials, and especially the CuCo 1:4 catalyst, showed synergic effect when used as catalyst on selective hydrogenation reaction of cinnamaldehyde.

5. Acknowledgments

The authors would like to thank Pardis Simon (UCCS) for her help in carrying out the work on the Surface Analysis facilities. The Chevreul Institute is thanked for its help in the development of this work through the ARCHI-CM project supported by the “Ministère de l’Enseignement Supérieur de la Recherche et de l’Innovation”, the region “Hauts-de-France”, the ERDF program of the European Union and the “Métropole Européenne de Lille.

6. References

1. L. Liu, A. Corma, Chem. Rev. 118 (2018) 4981–5079. <https://doi.org/10.1021/acs.chemrev.7b00776>

2. J.M. Campelo, D. Luna, R. Luque, J.M. Marinas, A.A. Romero, *ChemSusChem* 2 (2009) 18-45.
<https://doi.org/10.1021/acs.chemrev.7b00776>
3. B.M. Reddy, G.M. Kumara, I. Ganesh, A. Khana, *J. Molec.Catal. A* 247 (2006) 80-87.
<https://doi.org/10.1016/j.molcata.2005.11.026>
4. P. Mäki-Arvela, J. Hájek, T. Salmi, D.Yu. Murzin, *Appl. Catal. A* 292 (2005) 1-49.
<https://doi.org/10.1016/j.apcata.2005.05.045>
5. B. R. Cuenya, *Thin Solid Films*, 518(2010) 3127-3150. <https://doi.org/10.1016/j.tsf.2010.01.018>
6. S. Taghavi, E. Ghedini, F. Menegazzo, M. Signoretto, D. Gazzoli, D. Pietrogiacomini, A. Matayeva, Andrea Fasolini, Angelo Vaccari, Francesco Basile, G. Fornasari, *Processes* 8(7) (2020), 843-858.
<http://dx.doi.org/10.3390/pr8070843>
7. S. Chen, C. Ciotonea, A. Ungureanu, E. Dumitriu, C. Catrinescu, R. Wojcieszak, F. Dumeignil, S. Royer, *Catal. Today* 334 (2019) 48-58. <https://doi.org/10.1016/j.cattod.2019.01.064>
8. A. Rodriguez-Gomez, A. Caballero, *Mol Catal.* 449 (2018) 122-130.
<https://doi.org/10.1016/j.mcat.2018.02.011>
9. S. Todorova, J.L. Blin, A. Naydenov, B. Lebeau, H. Kolev, P. Gaudin, A. Dotzeva, R. Velinova, D. Filkova, I. Ivanova, L. Vidal, L. Michelin, L. Josien, K. Tenchev, *Catal. Today* 357 (2020) 602-612.
<https://doi.org/10.1016/j.cattod.2019.05.018>
10. S. Singh, R. Kumar, H.D. Setiabudia, S. Nandac, D.V.N. Vo, *Appl. Catal. A*. 559 (2018) 57-74.
<https://doi.org/10.1016/j.apcata.2018.04.015>
11. Y.W. Jiang, K. Chai, Y.Q. Wang, H.D. Zhang, W. Xu, W. Li, Y. Shi, *ACS Appl. Nano Mater.* 2 (2019) 4435-4442. <https://doi.org/10.1021/acsanm.9b00828>
12. T.W. van Deelen, Carlos Hernández Mejía, K. P. de Jong, *Nat. Catal.*, 2(11) (2019) 955-970.
<https://doi.org/10.1038/s41929-019-0364-x>
13. P. Munnik, M. Wolters, A. Gabrielsson, S. D Pollington, G. Headdock, J. H. Bitter, P. E. de Jongh, and K. P. de Jong, *J. Phys. Chem. C* 115 (2011) 14698-14706. <https://doi.org/10.1021/jp111778g>
14. R. Beerthuis, N.L. Visser, J.E.S. van der Hoeven, P. Ngene, J.M.S. Deeley, G.J. Sunley, K. P. de Jong, P.E. de Jongh, *J. Catal.* 394 (2021) 307-315. <https://doi.org/10.1016/j.jcat.2020.11.003>
15. A. Ungureanu, B. Dragoi, A. Chiriac, C. Ciotonea, S. Royer, D. Duprez, A. S. Mamede, E. Dumitriu, *ACS Appl. Mater. Interfaces* 5 (2013) 3010-3025. <https://doi.org/10.1021/am302733m>

16. B. Dragoi, A. Ungureanu, C. Ciotonea, A. Chiriac, S. Petit, S. Royer, E. Dumitriu, *Micropor. Mesopor. Mat.* 224 (2016) 176-189. <https://doi.org/10.1016/j.micromeso.2015.11.028>
17. M.L. Smith, A. Campos, J.J. Spivey, *Catal. Today* 182 (2012) 60-66.
<https://doi.org/10.1016/j.cattod.2011.07.026>
18. S. Deng, Wei Chu, H. Xu, L. Shi, L. Huang, J.; *Nat. Gas Chem.* 17 (2008) 369-373.
[https://doi.org/10.1016/S1003-9953\(09\)60011-6](https://doi.org/10.1016/S1003-9953(09)60011-6)
19. X. Ge, H. Sun, K. Dong, Y. Tao, Q. Wang, Y. Chen, G. Zhang, P. Cui, Y. Wang, Q. Zhang, *RSC Adv.*, 9 (2019) 14592-14598. <https://doi.org/10.1039/C9RA01927H>
20. Y. Yang, X. Qi, X. Wang, D. Lv, F. Yu, L. Zhong, H. Wang, Y. Sun, *Catal Today*, 270 (2016) 101-107.
<https://doi.org/10.1016/j.cattod.2015.06.014>
21. G.V. Deshmane, S.L. Owen, R.Y. Abrokwhah, D. Kuila, *J. Mol Catalysis A: Chem.* 408 (2015) 202–213.
<https://doi.org/10.1016/j.molcata.2015.07.023>
22. H. Wang, L. Zhou, M. Han, Z. Tao, F. Cheng, J. Chen, *J. Alloy Compd.* 651 (2015) 382-388.
<https://doi.org/10.1016/j.jallcom.2015.08.139>
23. R. Bagtachel, K. Boudjedien, I. Sebai, D. Meziani, M. Trari, *Appl. Physics A* 127 (2021) 60-67,
<https://doi.org/10.1007/s00339-020-04198-7>
24. G. Fierro, M. Lo Jacono, M. Inversi, R. Dragone, P. Porta, *Top Catal.* 10 (2000) 39- 48.
<https://doi.org/10.1023/a:1019151731177>
25. P. Stefanov, I. Avramova, D. Stoichev, N. Radic, B. Grbic, Ts. Marinova, *Appl. Surf. Sci.* 245 (2005) 65–72.
<https://doi.org/10.1016/j.apsusc.2004.09.120>
26. B.M. Abu-Zied, S.A. Soliman, S.E. Abdellah, *J. Ind. Eng. Chem.* 21 (2015) 814–821.
<https://doi.org/10.1016/j.jiec.2014.04.017>
27. R.P. Bonchev, T. Zheleva, S.C. Sevovem. *Mat.* 1990,2, 93-95. <https://doi.org/10.1021/cm00008a003>
28. S.C. Petitto, E.M. Marsh, Gregory A. Carson, M.A. Langell, *J. Mol. Catal. A:* 281 (2008) 48-58.
<https://doi.org/10.1016/j.molcata.2007.08.023>
29. C. Ciotonea, B. Dragoi, A. Ungureanu, C. Catrinescu, S. Petit, H. Alamdari, E. Marceau, E. Dumitriu, S. Royer, *Catal. Sci. Technol.*, 2017,7, 5448-5456. <https://doi.org/10.1039/C7CY00963A>
30. S. Shylesha, P. Mahendra Kapoor, R. Lekh. Juneja, P. Prinson Samuela, Ch. Srilakshmi, A.P. Singh, J. *Molec. Catal. A: Chem.* 301 (2009) 118-126. <https://doi.org/10.1016/j.molcata.2008.11.020>

- 31 P. N Rylande., D. R. Steele, Engelhard Minerals and Chemicals Corp., US 3 655 777, 1968
32. P. Gallezot and D. Richard, *Catal. Rev. Sci. Eng.* 40 (1998), 81-126.
<https://doi.org/10.1080/01614949808007106>
33. P. Claus, *Top. Catal.* 5 (1998) 51- 62, <https://doi.org/10.1023/A:1019177330810>
34. J.R.A. Sietsma, J.D. Meeldijk, M. Versluijs-Helder, A. Broersma, A. Jos van Dillen, P.E. de Jongh, K.P. de Jong, *Chem. Mater.* 20 (2008) 2921–2931. <https://doi.org/10.1021/cm702610h>
36. J.X. Flores-Lasluisa, J. Quílez-Bermejo, A.C. Ramírez-Pérez, F. Huerta, D. Cazorla-Amorós, E.Morallón, *Materials* 12 (2019) 1302-1315. <https://doi.org/10.3390/ma12081302>
37. C. Ciotonea, B. Dragoi, A. Ungureanu, A. Chiriac, S.Petit, S.Royer, E. Dumitriu, *Chem. Commun.*, 49 (2013), 7665-7669. <https://doi.org/10.1039/C3CC43197E>
38. Mark C. Biesinger, *Surf. Interf. Anal.* 49 (2017) 1325-1334. <https://doi.org/10.1002/sia.6239>Citations: 381
39. M.C. Biesinger, B.P. Payne, A.P. Grosvenor, L.W.M. Lau, A.R. Gerson, R. St, C. Smart, *Appl. Surf. Sci.* 257 (2011) 2717–2730. <https://doi.org/10.1016/j.apsusc.2010.10.051>
40. Y. Qi, Z. Yang, T. Chen, Y. Xi, J. Zhang, *Appl. Surf. Sci.* 501 (2020) 144165.
<https://doi.org/10.1016/j.apsusc.2019.144165>
41. A.J Marchi, D.A Gordo, A.F Trasarti, C.R Apesteguía, *Catalysis A: Chemical* 249, (2003), 53-67,
[https://doi.org/10.1016/S0926-860X\(03\)00199-6](https://doi.org/10.1016/S0926-860X(03)00199-6)